Available online at www.eccomasproceedia.org
Eccomas Proceedia SMART (2023) 1435-1446

ECCOMAS
Proceedia

X ECCOMAS Thematic Conference on Smart Structures and Materials
SMART 2023
D.A. Saravanos, A. Benjeddou, N. Chrysochoidis and T. Theodosiou (Eds)

ADVANTAGES OF THERMOMECHANICAL COUPLING IN SHAPE MEMORY ALLOY COMPONENTS APPLIED TO SPACECRAFT THERMAL CONTROL

Collette N. Gillaspie* **and Darren J. Hartl***

*Texas A&M University
Department of Aerospace Engineering
701 H.R. Bright Building 3141, College Station, TX 77843
e-mail: darren.hartl@tamu.edu

Key words: shape memory alloys, thermomechanical coupling, spacecraft, thermal control

Abstract. Human crewmember survival is essential to establishing an indelible presence on the Moon. Thus, crewed areas of spacecraft must remain within delicate temperature limits for human survival. Thermal control system (TCS) architecture relies upon radiative methods to reject excess heat during hot operational and/or environmental phases and preserve heat during cold, inactive phases. Traditionally, radiator configurations within heat rejection systems have consisted of static tube-and-fin geometries, which are restricted by the provision of power and surface area limitations. Such restrictions can be surpassed by means of the passively stimulated multifunctional response of shape memory alloys (SMAs) used to actuate a flexible radiator fin in response to a thermal stimulus, modifying system heat rejection to space. To evaluate the benefit of SMA-actuated thermal control, the operating envelope of a static rectangular-finned radiator-based TCS is compared to the extended operating envelope of an active morphing-finned radiator-based TCS during daytime lunar surface operations. Multiphysics finite element models simulate both TCS designs. The performance and efficacy of each design is quantified with (1) the ratio of the maximum to the minimum heat rejection rate collected during a simulated lunar south pole mission archetype and (2) the minimum working fluid temperature during the analysis. The active morphing-finned radiator-based TCS (1) accommodates varying heat loads and (2) prevents working fluid freezing, minimizing TCS complexity and enabling a single, non-toxic working fluid loop.

1 INTRODUCTION

To date, the problem of crewed spacecraft thermal control remained unsolved. In the 1984 Space Power workshop, NASA listed three advanced thermal technology goals toward which to focus its efforts: long-life heat rejection, versatile thermal acquisition and transport, and integrated thermal utility [1]. Captured within these specific aims was an environmentally sensing and self-regulating radiator system that can detect thermal energies and reorient its geometry accordingly [1]. Today, efficient thermal control system (TCS) heat rejection and storage is still low-maturity in terms of technology readiness and is therefore a NASA priority [2]. Despite external environmental and imposed operational heating conditions, a TCS must manage the

Peer-review under responsibility of the organizing committee of SMART 2023.
doi: 10.7712/150123.9915.444709

temperatures of spacecraft within certain limits [2]. As lunar south pole infrastructure logistics and Artemis III [3] itineraries solidify, the demand for a TCS that can maintain spacecraft thermal homeostasis escalates. Temperature fluctuations originate from heat sources internal to the spacecraft (e.g., astronaut metabolic output, equipment heat dissipation [4]) and external thermal radiation due to a wide range of lunar environments [5] stemming from critical mission contexts (e.g., low Earth orbit, trans-lunar coast, low lunar orbit, lunar surface operations [6]).

Current TCS heat rejection methods involve static, passive-structure radiators typically sized for two conditions: low-temperature radiators facing considerable backloading (i.e., absorbed radiative heat loads from the environment and surface-to-surface interactions) and high-temperature radiators facing moderate backloading [4]. Static, passive-structure radiators (e.g., a radiator configuration with flat, rectangular fins) fail when heat rejection requirements and environmental backloading vary vastly during a mission [7]. Since 2015 [8], investigators at Texas A&M University, NASA, Paragon Space Development Corporation, and The Boeing Company have sought to combat this conflicting exigence during missions requiring adaptable heat rejection. NASA Tipping Point Project funding [9] in 2019 supported the analytical, computational, and experimental research of a TCS that employs shape memory alloy (SMA) actuation. Versatile SMA materials replace complicated actuation system components (e.g., stepper motors, spring-loaded cables, gear systems) with a simple, active component that directly and reliably [10] couples the thermal and mechanical fields. Integrating SMAs into radiator fin construction converts a passive structure into a self-actuating and self-regulating active structure and enables the dynamic control of radiator geometry [11, 12]. The control of radiator geometry varies radiator view factor F, which is directly proportional to the radiative heat rejection rate $\dot{Q}$. SMA-induced view factor adjustment contributes to a key measure of radiator performance: a metric called turndown. In Eq. (1), turndown R is defined as the ratio of the maximum radiative heat rejection rate $\dot{Q}_{\max}$ to the minimum radiative heat rejection rate $\dot{Q}_{\min}$

$$R = \frac{\dot{Q}_{\max}}{\dot{Q}_{\min}} = \frac{\sigma\big(\sum \mathscr{A}_j F_{j\to\text{space}}\,\varepsilon_j\big)_{\max}\big(T^4_{\text{fin,max}} - T^4_{\text{sink}}\big)}{\sigma\big(\sum \mathscr{A}_j F_{j\to\text{space}}\,\varepsilon_j\big)_{\min}\big(T^4_{\text{fin,min}} - T^4_{\text{sink}}\big)}. \tag{1}$$

Turndown quantifies radiator heat rejection modulation during a mission. It may be subdivided into the following categories: geometric (i.e., variation in radiator view to space, captured by both area $\mathscr{A}$ and view factor F), surface (i.e., variation in emissivity ε), system (i.e., temperature variation inside the spacecraft T_{fin}), and environmental (i.e., temperature variation outside the spacecraft T_{sink}). Active morphing-finned (AMF) radiators succeed in addressing all four categories of turndown, unlike static rectangular-finned (SRF) radiators. To measure system turndown, prototypes of AMF radiator-based TCS technology have been subjected to temperature cycling tests in the NASA Johnson Space Center cold-walled high vacuum Chamber G [13, 14] and Chamber N [11, 15]. Additionally, a recent evaluation of AMF radiator-based TCS technology computed a simulation turndown ratio of 42.8:1 and a thermal vacuum chamber experiment turndown ratio of 8.9:1 [11].

Another performance metric in TCS evaluation is the minimum working fluid temperature. SMA elements (e.g., wires) in AMF radiators sense and monitor fin temperature and actuate fin motion. Fin motion modifies radiator view factor and resultant heat dissipation from a mechanically pumped fluid loop. As demonstrated later in this work, radiator fin vacillation

during a mission can prevent most coolants, even non-toxic high-freeze-point propylene glycol 50% in aqueous solution, from freezing. Working fluid freezing during cold environment traverse had not been a substantial issue for Space Shuttle missions and the International Space Station active thermal control system [16] because preceding TCS architecture incorporated two loops: one non-toxic, high-freeze-point coolant loop internal to the spacecraft and one toxic, low-freeze-point coolant loop external to the spacecraft, illustrated in Fig. 1a. An advantage of an AMF radiator-based TCS is the utilization of a single-loop TCS architecture with high-freeze-point, crew-safe working fluids, illustrated in Fig. 1b. Consequently, the effect of SMA-actuated fin vacillation could eliminate complications associated with an external, toxic, and low-freeze-point working fluid loop. These complications include a 25% mass increase [17], additional pumps with associated major and minor losses, heat transfer inefficiencies between the inner and outer working fluid loops, and a higher probability of working fluid loop leakage. In particular, a single-loop TCS architecture (cf. Fig. 1b) and radiator size reduction will decrease system mass and therefore launch costs.

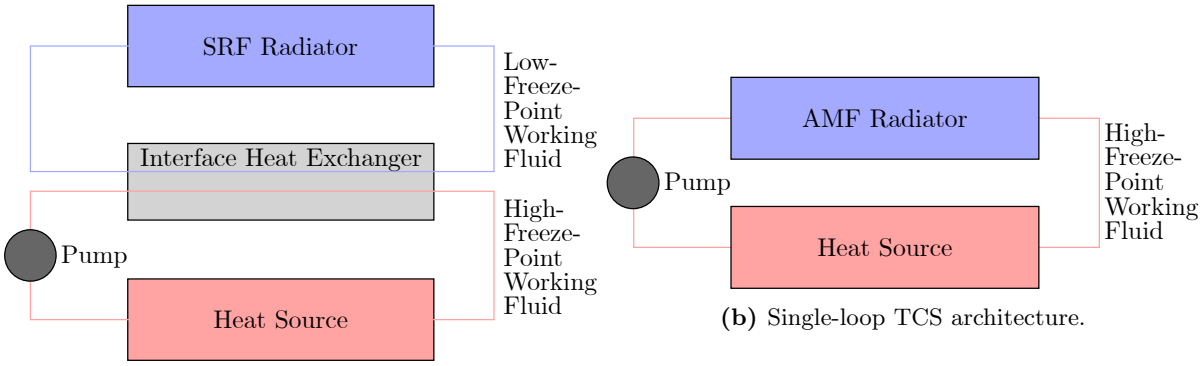

(a) Dual-loop TCS architecture.

(b) Single-loop TCS architecture.

Figure 1: Simplified TCS architecture schematics adapted from Lam et al. [4] and Nizio et al. [18].

Previous studies [19] have been performed to determine system-level sizing with an SRF radiator verification and a priori assumptions have driven past research [11, 12, 18, 20–23]. To date, no study has directly compared SMA-actuated, morphing-finned radiator performance to flat-finned radiator performance in the context of a single-loop TCS. Inspired by the Artemis III trajectory toward a human lunar south pole surface operations mission [24], such comparisons are conducted herein at the lunar south pole latitude of 70° S on the selenographic coordinate system (cf. Sect. 2.1). The presented self-actuating and self-regulating TCS employs SMAs to convert thermal energy into radiator fin reorientation, which has the dual effect of maintaining the working fluid above the freezing point and bounding the outlet temperature range to human spaceflight limits. Specifically, the metrics of turndown (cf. Sect. 3.1) and minimum working fluid temperature (cf. Sect. 3.2) compare the performance of an AMF radiator-based TCS to an SRF radiator-based TCS. Metric results provide substantial evidence that an AMF-based TCS will outperform an SRF-based TCS during a lunar south pole mission.

2 METHODOLOGY

2.1 Lunar South Pole Mission

Rugged lunar topography-induced radiance variations [25], a tenuous atmosphere (i.e., an exosphere), the insulating effects of surface regolith [26], and photometric property differences (i.e., albedo fluctuations) [27] are strongly correlated to the lunar daytime (i.e., 0600 to 1800 local solar time) temperature profile in Fig. 2. At latitude 70° S, sink temperatures[1] remain colder than working fluid temperatures. In this comparative study, TCS performance was measured over the first seven time increments (i.e., 0600 to 1200 local solar time) of the temperature profile provided in Fig. 2, as the profile is nearly symmetric and the effects of SMA hysteresis are not considered in this preliminary study.

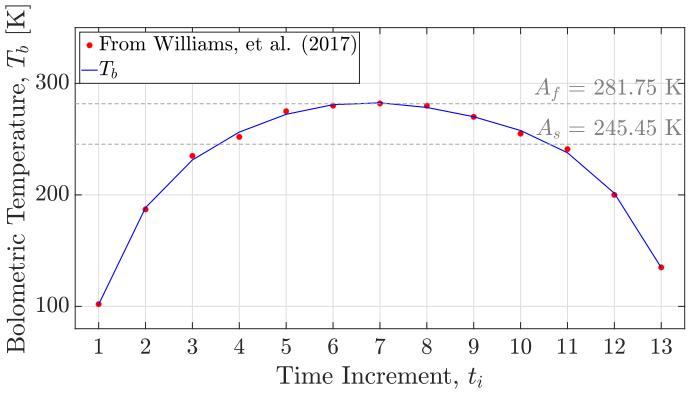

Figure 2: Lunar temperatures corresponding to 0600 local solar time t_1 through 1800 local solar time t_{13} at latitude 70° S approximated from spectrally integrated infrared radiation flux from lunar surface [25].

2.2 Model Characteristics

Two TCS models, the SRF radiator-based TCS and the AMF radiator-based TCS, were built and simulated in the Abaqus Finite Element Analysis software suite. Both models are thermally and mechanically symmetric about the yz-plane to reduce computational expense. The SRF radiator-based TCS and AMF radiator-based TCS models are pictured in Fig. 3a and Fig. 3b, respectively. A kinematic boundary condition to restrict rotation about z-axis for shell elements (i.e., comprising the fins as well as the AMF radiator end shields) tied to continuum elements (i.e., constituting the flow tubes) was also applied. A Dirichlet boundary condition holds constant the working fluid inlet temperature (i.e., $T = T_{\text{inlet}}$ at $z = 0$).

In the current study, the working fluid inlet was directly prescribed 289 K [19]. Forced convection and advective heat transfer from the working fluid inlet surface were simulated by imposing a mass flow rate per unit area in Abaqus. The user subroutine UMASFL permitted mass flow rate manipulation to investigate the effect of mass flow rate variation on the rate of radiant energy exchange for the SRF and AMF configurations. In the two TCS models,

[1] In direct sunlight in lunar vacuum, radiative heating is amplified, as radiation is reflected from lunar regolith in the infrared radiation band. In this study, it is assumed that bolometric temperature is equated to radiator sink temperature (i.e., $T_{\text{sink}} \approx T_b$).

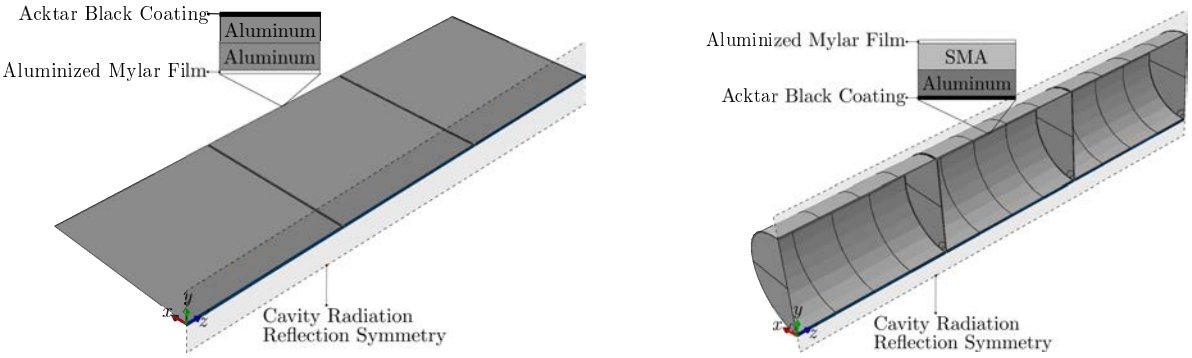

(a) SRF radiator-based TCS. **(b)** AMF radiator-based TCS.

Figure 3: TCS models in Abaqus showing geometry, material layup, and cavity radiation reflection symmetry plane.

propylene glycol 50% in aqueous solution is modeled in the UMASFL subroutine as turbulent[2] (i.e., $\mathrm{Re}_D = \rho v_{\mathrm{bulk}} 2R/\mu \geq 2300$) [28]. Experimentally, this would result in chaotic fluid velocity and pressure changes as well as increased fluid mixing [28]. In the model, only the non-parabolic velocity profile in the z-direction is considered. The Petukhov friction factor f for constant-property flow within a smooth tube wall and wall shear stress τ_w help characterize friction velocity $v^* = (\tau_w/\rho)^{1/2}$ [28]. Formulae for f and τ_w are given as

$$f = (1.82 \log_{10} \mathrm{Re}_D - 1.64)^{-2}, \quad \tau_w = \frac{f}{8}(\rho v_{\mathrm{bulk}}^2). \tag{2}$$

From the friction velocity v^* the dimensionless coordinate $y^+ = y v^* \rho/\mu$ may be retrieved where $y = R - r$, which determines Eq. (3): the three-layer universal velocity profile function v^+ by von Kármán [29].

$$v^+ = \frac{v}{v^*} = \begin{cases} y^+, & \text{if } 0 < y^+ \leq 5 \\ 5.0 \ln y^+ - 3.05, & \text{if } 5 < y^+ < 30 \\ 2.5 \ln y^+ + 5.5, & \text{if } y^+ \geq 30 \end{cases} \tag{3}$$

Near the tube wall (i.e., the viscous sublayer, $0 < y^+ \leq 5$), z-velocity flow follows a linear relationship, whereas a logarithmic relationship exists at locations away from the tube wall (i.e., the buffer layer and the turbulent region, $y^+ > 5$). Because UAMP sensor delegation is constrained to nodes, the outlet temperature T_{outlet} was specified as the center node of the working fluid. To simulate fluid mixing (e.g., installing turbulence promoters [30] within the tube), homogenize fluid temperatures throughout flow cross-sections, and mitigate nodal temperature differences at the surface, the thermal conductivity of the fluid k in Table 3 was artificially increased to 39400 W m^{-1} K^{-1}. Nodal temperature differences at the outlet surface were consequently mitigated, allowing for a z-local, single-node representation of the homogenized temperature and aiding in the UAMP sensor collection of T_{outlet}.

[2]N.B.: While mass flow rates of correspond to $\mathrm{Re}_D < 2300$, turbulence tripping via flow inserts was assumed for the purpose of heat transfer enhancement. Additionally, it was assumed that the correlation provided in Eq. (2) could be employed despite the possibility of intermittent turbulence at Reynolds numbers less than 10000.

2.3 Materials

As shown in Figs. 3a and 3b, radiator fins were modeled in Abaqus as composites. The fin surfaces, Acktar Black coating and aluminized Mylar polyester film, were not granted dedicated structural plies but were assigned emissivity values of 0.937 and 0.037, respectively [23]. As the radiators are significantly thin, fins were meshed with four-node, reduced integration shell elements (i.e., S4R).

Throughout the analysis, the SRF radiator-based TCS maintains a completely stationary configuration. Aluminum ply material properties for the SRF radiator-based TCS were chosen to mimic those of Heat Rejection Subsystem (HRS) radiators on the International Space Station. The external face sheets of the HRS radiators are composed of 6061-T6 aluminum [32]; these properties [31] were assigned to both aluminum plies (cf. Table 1). Indicated in the detail view of Fig. 3a, an Acktar Black coating emissivity $\varepsilon = 0.937$ was applied to the $+y$ fin surfaces, which have nearly a full view to space, and an aluminized Mylar film emissivity $\varepsilon = 0.037$ was applied to the $-y$ fin surfaces.

Table 1: 6061-T6 aluminum alloy model parameters [31].

Material Parameter	Value
E	6.89×10^{10} Pa
ν	0.33
ρ	2700 kg m^{-3}
c	896 J kg^{-1} K^{-1}
k	167 W m^{-1} K^{-1}

Illustrated in Fig. 3b, the second composite ply layer of the AMF radiator is denoted with an SMA material, as opposed to aluminum in Fig. 3a. This subset of active materials retains a previous configuration when exposed to sufficient thermomechanical energy [34]. The repeatable self-controlled actuation resulting from thermally driven phase transformation [34] adapts an AMF radiator-based TCS to an extensive range of thermal environments at zero power penalty [35]. For the purpose of computationally efficient modeling (i.e., avoiding contact interactions during mechanical and thermal simulations), the AMF radiator-based TCS considers the homogenization of SMA wire elements into a singular ply layer with properties presented in Table 2.

Table 2: SMA ply model parameters generated from constitutive model calibration tool [23] and compiled for the NiTi class of SMAs (i.e., ρ, c, k^A, and k^M) [33].

Material Parameter	Value
E^A	2.06×10^{10} Pa
E^M	1.19×10^{11} Pa
ν	0.33
A_s	245.45 K
A_f	281.75 K
M_s	228.15 K
M_f	203.55 K
ρ	6500 kg m^{-3}
c	490 J kg^{-1} K^{-1}
k^A	18 W m^{-1} K^{-1}
k^M	8.6 W m^{-1} K^{-1}

When cooperatively paired, the shape memory ply and the aluminum ply within the composite fin undergo cyclic actuation. During the heating stage of the mission (i.e., reverse phase transformation into austenite), the shape memory ply recovers initial tensile strain and uncurls the composite radiator fin into a semicircular shape. The view factor of the concave, 0.937-emissivity Acktar black surface [23] is consequently increased, expediting radiative heat transfer. Conversely, during a cooling stage of a mission (i.e., forward phase transformation into martensite), the shape memory ply relaxes as transformation strain is generated once again, which returns the composite radiator fin to a cylindrical closed shape. The view factor of the concave surface approaches zero, and the convex, 0.037-emissivity aluminized

Mylar surface [23] becomes increasingly exposed, impeding radiative heat transfer. Calibrated model parameters tested in thermal vacuum [23] and values collected from literature for density, specific heat, and thermal conductivity for the NiTi class of SMAs [33] are provided in Table 2.

In this first work comparing SRF and AMF radiators, the focus is placed on the implications of shape change during heating and not on the effects of hysteresis, which will be explored in future work. To simplify this study, a simple nonlinear thermal expansion model [36] is invoked to simulate thermally induced transformation. Given a simple statement for effective thermal strain, Eq. (4),

$$\epsilon^{th} = \alpha_{11}(T - A_s) \tag{4}$$

a nonlinear secant thermal expansion coefficient in the circumferential direction α_{11} must be defined such that the recovery response of the SMA is captured. Orthotropic thermal expansion values in the principal material directions (i.e., α_{11}, α_{22}, and α_{33}) are given in Eq. (5) as

$$\alpha_{11} = \begin{cases} 0, & \text{if } 0 < T \leq A_s \\ \alpha^* = \dfrac{-0.00036}{(A_f - A_s)}, & \text{if } A_s < T \leq A_f \\ \dfrac{-0.00036}{(T - A_s)}, & \text{if } T > A_f \end{cases}; \quad \forall\, T, \alpha_{22} = \alpha_{33} = 0. \tag{5}$$

While this simple effective thermal expansion coefficient method may be employed to predict mechanical fin response during heating [37], the operational temperature and heat rejection implications of hysteresis during the transformation cycle are not considered in the present work.

One of the key benefits of SME behavior in the SMA ply is the prevention of fluid frost formation. Previously, the case of working fluid frost formation has not been a point of concern for multi-loop TCS architecture (e.g., the International Space Station External Active Thermal Control System) operating in environments warmer than the freezing point of the external loop coolant (e.g., ammonia at freezing point ∼195 K [38]). However, spacecraft positioned within the lunar south pole region will face temperatures ranging from 102 K to 283 K [25]. SMA-actuated deployable-retractable radiators [39] that morph according to the current thermal environment mitigate the risk of working fluid freezing and may even enable the usage of non-toxic working fluids (i.e., propylene glycol 50% in aqueous solution at freezing point ∼239 K [40]) within a lighter, single-loop TCS.

To evaluate this potential benefit, a 50/50 propylene glycol/water (PGW) coolant solution [8] was chosen as the working fluid of the modeled TCS. In general, propylene glycol, with material properties [40] listed in Table 3, is considered less toxic than ethylene glycol [41], which has been employed as the TCS working fluid in previous studies [11]. Because the working fluid domain must be included in a static stress analysis (cf. Sect. 2.4), artificial elastic properties

Table 3: 50/50 PGW working fluid model parameters of density ρ, specific heat c, thermal conductivity k, and dynamic viscosity μ [40].

Material Parameter	Value
ρ	1038 kg m^{-3}
c	3559 J kg^{-1} K^{-1}
k	0.394 W m^{-1} K^{-1}
μ	6.264 $\times 10^{-3}$ kg m^{-1} s^{-1}

sufficient to prevent numerical instabilities were assigned to 50/50 PGW. Here, the elastic modulus of stiff polyethylene glycol hydrogels was assigned (i.e., $E = 1 \times 10^6$ Pa) [42].

2.4 Partitioned Framework

As the thermal and mechanical responses of SMAs are highly interlinked, effective thermal expansion coefficient method implementation and consequent TCS performance evaluation requires a fully coupled thermal-stress analysis. However, to date the Abaqus toolset has not provided the capability of analyzing cavity radiation effects (i.e., the calculation of $F_{j\to\text{space}}$ in Eq. (1) at each point). At present, Abaqus exclusively computes cavity radiation between static bodies. To capture the response of the actuating material, a partitioned framework [43] (cf. Fig. 4) was developed by Bertagne [20, 21] and extended herein.

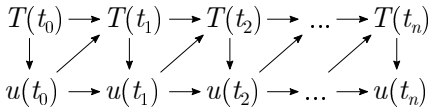

Figure 4: Partitioned framework to simulate TCS thermal-stress analysis.

The framework is composed of heat transfer steps and static stress steps. Heat transfer steps determine the distribution of temperatures in a body due to conduction and boundary radiation; static stress steps determine nodal displacements of a body while neglecting inertia effects. The quasi-static response is computed incrementally; at each increment t_i, a heat transfer analysis executes, followed by a subsequent static stress analysis. In the initial thermal step of the analysis procedure, a predefined temperature field that ensures convergence and initiates reverse transformation is assigned to the model (i.e., $T(t_0)$=253 K [11]). In the subsequent structural step, corresponding nodal temperatures from the initial thermal step are mapped onto the model as a predefined field. Differences between applied and initial temperatures induce thermal contraction in the SMA ply.

Thermal strain ϵ^{th} proportional to the temperature difference produces a displacement field (i.e., $u(t_0)$). Previous analyses of the adaptive TCS informed the designated thermal strain value (i.e., $\epsilon^{th} = -0.00036$). Successive data transmission (i.e., temperatures $T(t_i)$ from thermal steps and displacements $u(t_i)$ from structural steps) continues in this manner for increments t_1 through t_7, which are correlated to lunar sink temperatures at 70° S from 0600 to 1200 local solar time (cf. 2). Following the initial heat transfer analysis, a collection of solid element faces and shell element surfaces (i.e., facets) with a specified external medium temperature (i.e., an open cavity) primarily drives heat transfer. Typically, an open cavity definition in Abaqus permits a constant external medium temperature value. However, employing the sequentially coupled thermal-stress framework, an external environment represented in Fig. 2 was modeled.

3 RESULTS AND DISCUSSION

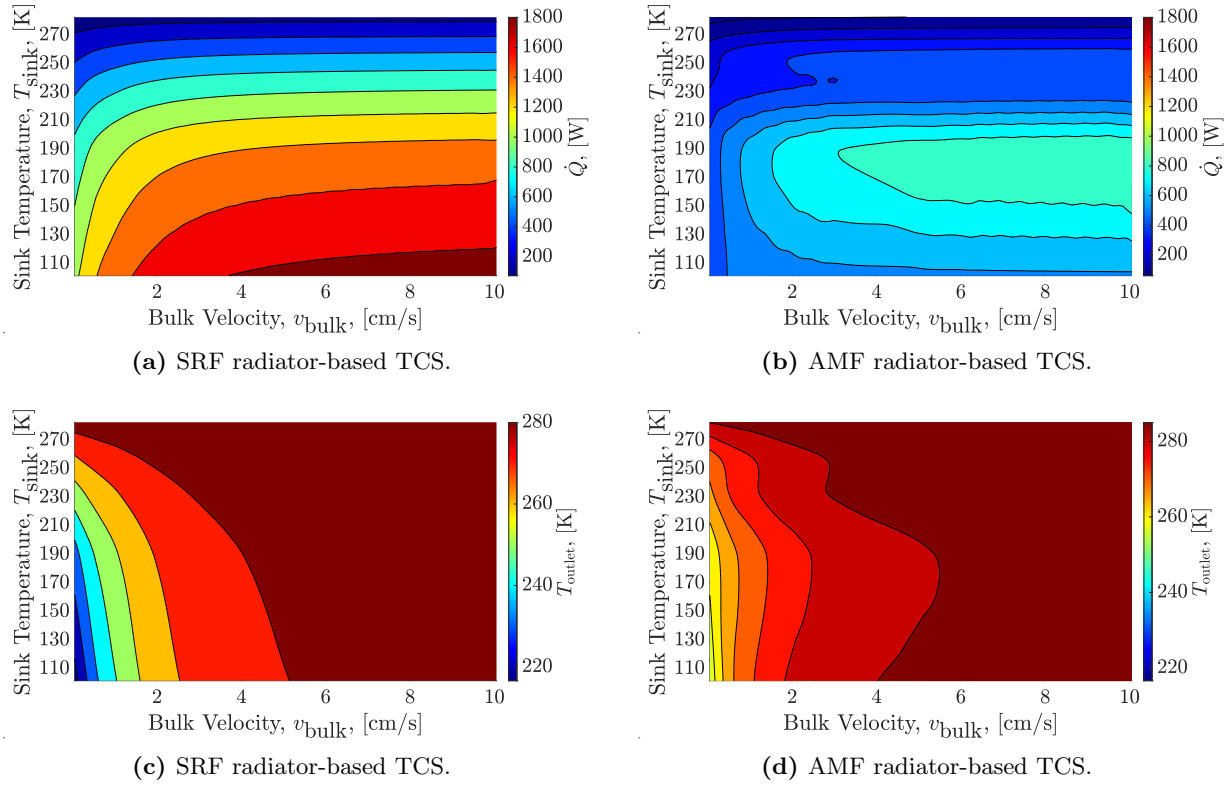

(a) SRF radiator-based TCS.

(b) AMF radiator-based TCS.

(c) SRF radiator-based TCS.

(d) AMF radiator-based TCS.

Figure 5: Filled contour plots displaying the isolines of matrices $\dot{Q}$ and T_{outlet}.

3.1 Turndown

Figures 5a and 5b display the three-dimensional contour plots of isolines indicating the radiative heat transfer rate $\dot{Q}$ from the SRF and AMF radiator configurations, respectively. Heat rate values were doubled to represent heat transfer from a full-sized TCS (i.e., mirroring the symmetry models presented in Fig. 3 across the yz plane). Data plotted stems from the cubic interpolation of a surface defined by the bulk velocity of the working fluid v_{bulk} and sink temperatures T_{sink} from time increment t_1 to t_7 in Fig. 2. At each bulk velocity, TCS heat rejection was evaluated and collected from 0600 to 1200 local solar time. In Fig. 5a, the $\dot{Q}$ distribution behaves as expected. At higher sink temperatures, lower rates of heat transfer are rejected from the radiators. At lower sink temperatures, higher rates of heat transfer are rejected from the radiators. Working fluid bulk velocities faster than $v_{\text{bulk}} = 4$ cm/s do not seem to affect the rate of heat rejection at the same sink temperature. The highest ratio of the maximum to the minimum heat rejection rate collected during a simulated lunar south pole mission archetype corresponded to $v_{\text{bulk}} = 0.05$ cm/s at $R = 15.60 : 1$. While a turndown ratio equal to 15.60:1 is largely viewed as satisfactory, Sect. 3.2 demonstrates the importance of the second metric, the minimum working fluid temperature during the analysis, to TCS assessment. Generally, compared to Fig. 5a, the AMF radiator-based TCS in Fig. 5b emits radiation at lower rates than

the SRF radiator-based TCS[3]. This quality is especially advantageous in cold sink temperature cases (i.e., 0600 and 0700 local solar time), as it mitigates the chance of working fluid freezing. Additionally, distinct sink temperature values yield similar values of $\dot{Q}$ at the same bulk velocity. This result reveals the power of passive configuration change, as cold external temperatures can garner analogous heat rejection rate values to external environments. The highest ratio of the maximum to the minimum heat rejection rate collected during a simulated lunar south pole mission archetype corresponded to $v_{\text{bulk}} = 10.05$ cm/s at $R = 8.43 : 1$. This turndown value approaches the 2015 NASA Thermal Management Systems turndown ratio goal of 12:1 [7].

3.2 Working Fluid Outlet Temperature

Figures 5c and 5d display the three-dimensional contour plots of isolines indicating averaged working fluid outlet temperatures T_{outlet} for the SRF and AMF radiator configurations, respectively. Working fluid outlet temperatures correspond to the lowest temperatures in the working fluid (i.e., propylene glycol 50% in aqueous solution) with freezing point ∼239 K [40]. It may be easily seen in Fig. 5c that the SRF radiator-based TCS freezes the fluid at low bulk velocities and low sink temperatures. Specifically, the SRF radiator-based TCS freezes 50/50 PGW at bulk velocities $v_{\text{bulk}} = 0.05$ and 0.55 cm/s at the lunar sink temperature corresponding to 0600 local solar time with $T_{\text{outlet}} = 216.6$ and 238.2 K, respectively. Unlike the SRF radiator-based TCS in Fig. 5c, the AMF radiator-based TCS in Fig. 5d never freezes 50/50 PGW. Even at low values of v_{bulk} and T_{sink}, radiator morphing prevents excessive heat dissipation from the working fluid and thus augments the feasibility of the single-loop TCS architecture (cf. Fig. 1b).

4 CONCLUSIONS

In this study, the performance and efficacy of an SRF radiator-based TCS and an AMF radiator-based TCS were quantified in Sect. 3.1 with (1) turndown and in Sect. 3.2 with (2) the minimum working fluid outlet temperature during a simulated lunar mission at latitude 70° S. As determined from their turndown ratios, both TCS designs can accommodate varying heat loads. However, the application of thermomechanical coupling in SMA components demonstrates the ability of an AMF radiator-based TCS to mitigate transient and spatial variations internal and external to spacecraft. This application is manifested in Fig. 5d, which indicates that the AMF radiator-based TCS freezes the working fluid at no point during the investigated lunar surface mission. Thus, AMF radiator-based thermal control could decommission dual-loop TCS architecture and, with it, associated mass and launch cost savings for future missions.

5 ACKNOWLEDGMENTS

The authors would like to extend their appreciation for the proofreading efforts of Dr. Debra McKeown and Patrick Gillaspie.

References

[1] R. C. Parish, "Thermal Management Technology Status," in *Space Power: NASA CP-2352*, D. T. Bernatowicz *et al.*, Eds. Cleveland: National Aeronautics and Space Administration, 4 1984, pp. 189–203.

[2] National Aeronautics and Space Administration, "2020 NASA Technology Taxonomy," NASA, Washington, D.C., Tech. Rep., 2020. [Online]. Available: https://www.nasa.gov/sites/default/files/atoms/files/2020_nasa_technology_taxonomy.pdf

[3] Convergence issues suspended analysis at bulk velocities $v_{\text{bulk}} = 3.55, 4.05, 4.55$, and 5.55 cm/s. Data robustness in this bulk velocity region is therefore hindered.

[3] S. Creech *et al.*, "Artemis: An Overview of NASA's Activities to Return Humans to the Moon," in *IEEE Aerospace Conference Proceedings*, vol. 2022-March. IEEE Computer Society, 2022.

[4] D. G. Gilmore, Ed., *Spacecraft Thermal Control Handbook, Volume I: Fundamental Technologies*. Washington, D.C.: American Institute of Aeronautics and Astronautics, Inc., 12 2002.

[5] M. Harris *et al.*, "Spacecraft Radiation Torques," National Aeronautics and Space Administration, Washington, D.C., Tech. Rep. October, 10 1969. [Online]. Available: https://ntrs.nasa.gov/api/citations/19710014836/downloads/19710014836.pdf

[6] R. A. Stephan, "Overview of the Altair Lunar Lander Thermal Control System Design and the Impacts of Global Access," in *41st International Conference on Environmental Systems 2011, ICES 2011*. American Institute of Aeronautics and Astronautics Inc., 2011, pp. 1–13.

[7] National Aeronautics and Space Administration, "NASA Technology Roadmaps, TA 14: Thermal Management Systems," NASA, Washington, D.C., Tech. Rep. July, 7 2015. [Online]. Available: https://www.nasa.gov/sites/default/files/atoms/files/2015_nasa_technology_roadmaps_ta_14_thermal_management_final.pdf

[8] T. J. Cognata *et al.*, "A Morphing Radiator for High-Turndown Thermal Control of Crewed Space Exploration Vehicles," in *23rd AIAA/AHS Adaptive Structures Conference*, no. January. Kissimmee: American Institute for Aeronautics and Astronautics, 1 2015, pp. 1–12.

[9] L. Haas, "Paragon Space Development Corporation® wins $2 Million Dollar Contract under NASA Tipping Point Program," Paragon Space Development Corporation, Tucson, Tech. Rep., 11 2019. [Online]. Available: https://www.paragonsdc.com/wp-content/uploads/2019/11/NASA_Tipping_Point_Press_Release_Nov_2019.pdf

[10] D. J. Hartl *et al.*, "Aerospace Applications of Shape Memory Alloys," *Proceedings of the Institution of Mechanical Engineers, Part G: Journal of Aerospace Engineering*, vol. 221, no. 4, pp. 535–552, 2007.

[11] D. Miller *et al.*, "Shape Memory Alloys for Regulating TCS in Space (SMARTS): System Design and Thermal Vacuum," in *51st International Conference on Environmental Systems*. Saint Paul: ICES Organization, 7 2022, pp. 1–15. [Online]. Available: https://hdl.handle.net/2346/89803

[12] S. P. Nevin *et al.*, "Shape Memory Alloys for Regulating TCS in Space (SMARTS): Validated Multiphysical Modeling and Design Optimization of Morphing Composite Radiators," in *51st International Conference on Environmental Systems*. St. Paul: ICES, 7 2022, pp. 1–15. [Online]. Available: https://hdl.handle.net/2346/89754

[13] C. L. Bertagne, *Experimental Evaluation of an Analysis Framework for Simulating the Coupled Behavior of Shape Memory Alloy-Based Morphing Radiators [MS thesis]*. College Station: Texas A&M University Department of Aerospace Engineering, 8 2016. [Online]. Available: https://oaktrust.library.tamu.edu/bitstream/handle/1969.1/158032/BERTAGNE-THESIS-2016.pdf?sequence=1&isAllowed=y

[14] P. P. Walgren, *Towards High-Turndown-Ratio Shape Memory Alloy Driven Morphing Space Radiators: Manufacturing Methods, Computational Modeling, and Prototype Demonstration*. College Station: Texas A&M University Department of Aerospace Engineering, 5 2019. [Online]. Available: https://oaktrust.library.tamu.edu/bitstream/handle/1969.1/185061/WALGREN-THESIS-2019.pdf?sequence=1&isAllowed=y

[15] S. P. Nevin, *Combined Thermal and Structural Modeling and Design of a Shape Memory Alloy Driven Morphing Space Radiator [MS thesis]*. College Station: Texas A&M University Department of Aerospace Engineering, 12 2021. [Online]. Available: https://oaktrust.library.tamu.edu/bitstream/handle/1969.1/196368/NEVIN-THESIS-2021.pdf?sequence=1&isAllowed=y

[16] E. K. Ungar, "Spacecraft Radiator Freeze Protection Using a Regenerative Heat Exchanger with Bypass Setpoint Temperature Control," in *38th International Conference on Environmental Systems*, 38st International Conference on Environmental Systems. San Francisco: ICES, 6 2008, pp. 1–12. [Online]. Available: http://hdl.handle.net/2346/73011

[17] D. A. Ochoa *et al.*, "A Comparison Between One-and Two-Loop ATCS Architectures Proposed for CEV," *SAE International Journal of Aerospace*, vol. 4, no. 1, pp. 344–350, 7 2009.

[18] P. A. C. Nizio *et al.*, "Fabrication and Characterization of a Shape Memory Alloy Driven Composite Morphing Radiator Prototype," in *X ECCOMAS Thematic Conference on Smart Structures and Materials*, D. A. Saravanos, A. Benjeddou, N. Chrysochoidis, and T. Theodosiou, Eds., Patras, 7 2023, pp. 1–11.

[19] L. Erickson *et al.*, "Approach for Sizing and Turndown Analysis of a Variable Geometry Spacecraft Radiator," National Aeronautics and Space Adminstration, Houston, Tech. Rep., 8 2017.

[20] C. L. Bertagne *et al.*, "Testing and Analysis of a Morphing Radiator Concept for Thermal Control of Crewed Space Vehicles," *Applied Thermal Engineering*, vol. 124, pp. 986–1002, 2017.

[21] ——, "Coupled Behavior of Shape Memory Alloy-Based Morphing Spacecraft Radiators: Experimental Assessment and Analysis," *Smart Materials and Structures*, vol. 27, no. 6, 5 2018.
[22] P. P. Walgren *et al.*, "Development and Testing of a Shape Memory Alloy-Driven Composite Morphing Radiator," *Shape Memory and Superelasticity*, vol. 4, no. 1, pp. 232–241, 2018. [Online]. Available: https://doi.org/10.1007/s40830-018-0147-2
[23] ——, "Design, Experimental Demonstration, and Validation of a Composite Morphing Space Radiator," *Journal of Composite Materials*, vol. 0, no. 0, pp. 1–16, 12 2022.
[24] D. Elburn, "Artemis III: NASA's First Human Mission to the Lunar South Pole," 1 2023. [Online]. Available: https://www.nasa.gov/feature/artemis-iii
[25] J. P. Williams *et al.*, "The Global Surface Temperatures of the Moon as Measured by the Diviner Lunar Radiometer Experiment," *Icarus*, vol. 283, pp. 300–325, 2 2017.
[26] H. Haack *et al.*, "Effects of Regolith/Megaregolith Insulation on the Cooling Histories of Differentiated Asteroids," *Journal of Geophysical Research*, vol. 95, no. B4, pp. 5111–5124, 1990.
[27] G. D. Racca, "Moon surface thermal characteristics for moon orbiting spacecraft thermal analysis," *Planetary and Space Science*, vol. 43, no. 6, pp. 835–842, 6 1995.
[28] A. F. Mills and C. F. M. Coimbra, *Heat Transfer*, 3rd ed., W. Stenquist, Ed. San Diego: Temporal Publishing, LLC, 6 2016.
[29] T. von Kármán, "The Analogy Between Fluid Friction and Heat Transfer," *Transactions of the American Society of Mechanical Engineers*, vol. 61, no. 8, pp. 705–710, 11 1939. [Online]. Available: http://asmedigitalcollection.asme.org/fluidsengineering/article-pdf/61/8/705/6988080/705_1.pdf
[30] J. G. Knudsen *et al.*, *Fluid Dynamics and Heat Transfer*, M. S. Peters, Ed. New York: McGraw-Hill Book Company, Inc., 1 1958.
[31] L. MatWeb, "Aluminum 6061-T6; 6061-T651," 2023. [Online]. Available: https://www.matweb.com/search/DataSheet.aspx?MatGUID=b8d536e0b9b54bd7b69e4124d8f1d20a&ckck=1
[32] J. A. Oren *et al.*, "Space Station Heat Rejection Subsystem Radiator Assembly Design and Development," *Journal of Aerospace*, vol. 104, pp. 1086–1095, 1995. [Online]. Available: https://www.jstor.org/stable/44612020
[33] K. Otsuka *et al.*, *Shape Memory Materials*. Cambridge: Cambridge University Press, 1998.
[34] D. C. Lagoudas, Ed., *Shape Memory Alloys: Modeling and Engineering Applications*, 1st ed. New York: Springer Science+Business Media, LLC, 7 2008.
[35] C. M. Jackson *et al.*, "55-Nitinol—The Alloy With a Memory: Its Physical Metallurgy, Properties, and Applications," NASA, Washington, D.C., Tech. Rep., 1972. [Online]. Available: https://ntrs.nasa.gov/api/citations/19720022818/downloads/19720022818.pdf
[36] T. L. Turner *et al.*, "Finite Element Analysis of the Random Response Suppression of Composite Panels at Elevated Temperatures Using Shape Memory Alloy Fibers," in *Collection of Technical Papers - AIAA/ASME/ASCE/AHS/ASC Structures, Structural Dynamics and Materials Conference*, vol. 1. AIAA, 1994, pp. 136–146.
[37] ——, "Analysis of SMA hybrid composite structures in MSC.Nastran and ABAQUS," *Journal of Intelligent Material Systems and Structures*, vol. 18, no. 5, pp. 435–447, 5 2007.
[38] S. S. Zumdahl, "Ammonia," Cambridge, 12 2022. [Online]. Available: https://www.britannica.com/science/ammonia
[39] J. W. Leach *et al.*, "Flexible Deployable-Retractable Space Radiators," in *AIAA 12th Thermophysics Conference*. Albuquerque: American Institute for Aeronautics and Astronautics, 6 1977, pp. 1–11.
[40] The Engineering ToolBox, "Propylene Glycol based Heat-Transfer Fluids," 2003. [Online]. Available: https://www.engineeringtoolbox.com/propylene-glycol-d_363.html
[41] J. S. LaKind *et al.*, "A Review of the Comparative Mammalian Toxicity of Ethylene Glycol and Propylene Glycol," *Critical Reviews in Toxicology*, vol. 29, no. 4, pp. 331–365, 1999.
[42] K. W. Kolewe *et al.*, "Bacterial Adhesion Is Affected by the Thickness and Stiffness of Poly(ethylene glycol) Hydrogels," *ACS Applied Materials and Interfaces*, vol. 10, no. 3, pp. 2275–2281, 1 2018.
[43] K. C. Park *et al.*, "Partitioned Transient Analysis Procedures for Coupled-Field Problems: Accuracy Analysis," *Journal of Applied Mechanics*, vol. 47, no. 4, pp. 919–926, 12 1980. [Online]. Available: http://asmedigitalcollection.asme.org/appliedmechanics/article-pdf/47/4/919/5878400/919_1.pdf